

AGNs are not that cool:
revisiting the intrinsic AGN far-infrared spectral energy distribution

JUN XU,^{1,2} MOUYUAN SUN,^{1,2,3} AND YONGQUAN XUE^{1,2}

¹CAS Key Laboratory for Research in Galaxies and Cosmology, Department of Astronomy, University of Science and Technology of China, Hefei 230026, China; ericsun@ustc.edu.cn; xuey@ustc.edu.cn

²School of Astronomy and Space Science, University of Science and Technology of China, Hefei 230026, China

³Department of Astronomy, Xiamen University, Xiamen, Fujian 361005, China

(Revised Draft: March 24, 2020)

ABSTRACT

We investigate the intrinsic spectral energy distribution (SED) of active galactic nuclei (AGNs) at infrared (IR) bands with 42 $z < 0.5$ optically luminous Palomar Green survey quasars through SED decomposition. We decompose the SEDs of the 42 quasars by combining an AGN IR template library (Siebenmorgen et al. 2015) that covers a wide range of the AGN parameter space with three commonly used galaxy template libraries. We determine the median AGN SED from the best-fitting results. The far-IR (FIR) contribution of our median AGN SED is significantly smaller than that of Symeonidis et al. (2016), but roughly consistent with that of Lyu & Rieke (2017). The AGN IR SED becomes cooler with increasing bolometric luminosity, which might be due to that more luminous AGNs might have stronger radiative feedback to change torus structures and/or their tori might have higher metallicities. Our conclusions do not depend on the choice of galaxy template libraries. However, since the predicted polycyclic aromatic hydrocarbon (PAH) emission line flux is galaxy template-dependent, cautions should be taken on deriving galaxy FIR contribution from PAH fluxes.

Keywords: galaxies: active — infrared: galaxies — quasars: general

1. INTRODUCTION

It has been a common view that supermassive black holes (SMBHs) lie at the centers of typical massive galaxies. SMBHs swallow nearby gas through accretion disks (thereby being active galactic nuclei —AGNs) and their hosts form stars from cold gas at large scales. In this scenario, SMBHs become more massive and the accreted material radiates across a wide range of the electromagnetic spectrum. This is known as the quasar phase. According to the unified model (e.g., Antonucci 1993; Urry & Padovani 1995), AGNs are believed to be surrounded by dusty tori (e.g., Tristram et al. 2007). The dusty torus can absorb AGN UV/optical emission and re-radiate in the near-infrared, middle-infrared (MIR) and far-infrared (FIR) bands. The IR emission from the heated dusty torus usually peaks at MIR bands (e.g., Antonucci 1993) and turns over at $\sim 20\text{--}70\ \mu\text{m}$ (e.g., Netzer et al. 2007, ; Mullaney et al. 2011, hereafter M11).

AGNs can have significant influence on their hosts (i.e., AGN feedback; see e.g., Silk, & Rees 1998; King 2003; Fabian 2012) by strong multi-band radiation, multi-scale and multi-phase winds (e.g., Blandford & Payne 1982; Murray et al. 1995; Reynolds et al. 1997; Proga & Kallman 2004; Trump et al. 2006; Richards et al. 2011; Yuan et al. 2012; Cao & Spruit 2013; Tombesi et al. 2013; Filiz Ak et al. 2014; Grier et al. 2015; Gu 2015; Mou et al. 2017; Sun et al. 2018c, 2019; He et al. 2019) and/or relativistic jets (e.g., McNamara

et al. 2000). They can heat the interstellar medium (ISM) and/or eject the ISM and thereby reduce or even quench star formation in the host galaxies. Such a process might be able to explain the well-established $M_{\text{BH}} - \sigma$ (e.g., Ferrarese & Merritt 2000; Gebhardt et al. 2000; Tremaine et al. 2002; Kormendy & Ho 2013) and $M_{\text{BH}} - M_{\text{bulge}}$ (e.g., Kormendy & Richstone 1992; Magorrian et al. 1998; Häring & Rix 2004; Gültekin et al. 2009) scaling relations. To reveal the physical nature of the relations between SMBHs and their hosts, we should accurately measure the properties of AGNs (e.g., M_{BH} , accretion rate) and their host galaxies (e.g., star-formation rate, stellar mass) across cosmic history (e.g., Sun et al. 2015).

Star-formation rates (SFRs) are often measured (for a review, see Kennicutt 1998) by the total luminosity of ultraviolet (UV) emission of a galaxy or some recombination lines (e.g., H α). However, such estimators can be strongly contaminated by AGN emission. Stellar UV emission might also be absorbed by dusty clouds in galaxies. Unlike AGN emission, the stellar emission is usually much fainter. Thus, the average dust temperature is much cooler (e.g., Elvis et al. 1994; Richards et al. 2006; Netzer et al. 2007; Mullaney et al. 2011) and the re-radiated IR emission peaks at FIR bands (e.g., Dale & Helou 2002). Consequently, it has been suggested that FIR bands provide a clean window for measuring star-formation activities of host galaxies (e.g., Page et al. 2012; Harrison et al. 2012).

However, it was claimed (Symeonidis et al. 2016, hereafter S16) that the AGN emission in FIR bands is not negligible; without properly removing the AGN contamination, SFRs of many AGN hosts are significantly overestimated. S16 used a sample of 47 broad-line, luminous (the luminosity at 5100 \AA $L_{5100} > 10^{43.5} \text{ erg s}^{-1}$), $z < 0.18$, radio-quiet quasars from the Palomar Green survey (hereafter PG quasars; Schmidt & Green 1983). By using the archival data in the $0.4\text{--}500 \mu\text{m}$ range, S16 constructed the IR spectral energy distributions (SEDs). They derived the stellar contribution by matching the strength of $11.3 \mu\text{m}$ polycyclic aromatic hydrocarbon (PAH) feature with the galaxy template library of Dale & Helou (2002, hereafter DH02), i.e., selecting the galaxy template with the $11.3 \mu\text{m}$ PAH strength that is closest to the observed value. S16 then subtracted the average stellar contribution from the average PG quasar SED, resulting in the intrinsic AGN IR SED. Their intrinsic AGN IR SED is more luminous at FIR bands (by ~ 0.5 dex; i.e., the average dust temperature is much cooler) than those of previous works (e.g. Netzer et al. 2007, M11) for fixed $20 \mu\text{m}$ emission. Meanwhile, S16 found that AGNs with different $11.3 \mu\text{m}$ PAH luminosities tend to share the same FIR profile. This result is also incompatible with that of M11 who found that luminous AGNs tend to have a lower ratio of FIR emission to the total IR emission (see M11 Figure 6). S16 argued that the cool FIR emission could be a result of AGN UV/optical emission heating up the galactic-scale dust. If correct, the S16 results indicate that our understanding of star formation in AGN hosts would be substantially modified.

The DH02 galaxy template library is constructed as follows. Dale et al. (2001) developed a new phenomenological model characterized by a single parameter $f_{\nu}^{60 \mu\text{m}} / f_{\nu}^{100 \mu\text{m}}$ for normal star-forming galaxies. The models were constrained by *Infrared Astronomical Satellite* (IRAS) and *Infrared Space Observatory* (ISO) broadband photometric data of 69 normal galaxies with different IR luminosities. They replaced the Desert et al. (1990) PAH emission profiles with actual data from ISO. Their spectra extending up to $11 \mu\text{m}$ show an invariant shape regardless of their infrared-to-blue ratios. This indicates that there is no prominent $9.7 \mu\text{m}$ silicate absorption in their SEDs. Later, DH02 modified the FIR/submillimeter dust emissivity in the models to consider different radiation-field intensities and to match the long-wavelength (i.e., $\sim 100\text{--}800 \mu\text{m}$) data; then, they derived a commonly used galaxy template library. After that, Dale et al. (2014, hereafter DH14) updated the star-forming galaxy template library by considering the new *Spitzer* high-quality Infrared Spectrograph (IRS¹) spectra. Their new templates also contain an AGN component whose relative strength can be varied. In this work, we set the templates to zero AGN contribution. Meanwhile, Rieke et al. (2009, hereafter R09) assembled a galaxy template library by using a sample of eleven local luminous IR galaxies (LIRGs)

and ultra-luminous IR galaxies (ULIRGs). They constructed the near- to mid-IR profile (including the PAH and silicate features) by taking advantage of *Spitzer* IRS spectra (Houck et al. 2004) and ISO (Rigopoulou et al. 1999) spectra. At FIR bands, a modified blackbody model was fitted to the FIR and submillimeter photometry of each galaxy. In contrast to Dale & Helou (2002) and Dale et al. (2014), the $9.7 \mu\text{m}$ silicate absorption feature is included in the R09 library.

Recently, Lani et al. (2017) and Lyu & Rieke (2017, hereafter L17) checked the result of S16 by following the S16 PAH strength based method. However, they failed to obtain the AGN FIR SED of S16. Unlike S16, Lani et al. (2017) (who also used the DH02 templates) normalized the individual galaxy-emission-subtracted SEDs at $20 \mu\text{m}$ before deriving the average AGN SED (see also Section 4.1). L17 used the R09 templates instead, and took advantage of Elvis et al. (1994) sample, then used the relation between the $11.3 \mu\text{m}$ PAH equivalent width and the $25 \mu\text{m}$ to $60 \mu\text{m}$ or $24 \mu\text{m}$ to $70 \mu\text{m}$ flux ratio to estimate FIR contribution of star formation in Elvis et al. (1994). L17 argued that the stellar contribution would be biased to low values if the DH02 templates were adopted for PG quasars. This is because, as pointed out by L17, the $11.3 \mu\text{m}$ PAH line may overlap with the $9.7 \mu\text{m}$ silicate absorption feature. If the $9.7 \mu\text{m}$ silicate absorption is strong and ignored, the measured $11.3 \mu\text{m}$ PAH flux will be smaller than the true flux. As a result, the stellar emission inferred from the $11.3 \mu\text{m}$ PAH flux will also be underestimated. In addition, M11 constructed the AGN IR SED in an empirical way: first, they assumed that the AGN IR SED can be described by a modified blackbody function; second, they adopted this modified blackbody function (with unknown parameters, e.g., the blackbody temperature) and five starburst galaxy templates to simultaneously fit the IRS spectra and IRAS data of 11 *Swift*-BAT AGNs. The mean of the best-fitting AGN SEDs is also inconsistent with that of S16 (see Section 4).

In this work, we aim to check the result of S16 via a two-component (i.e., a galaxy component plus an AGN component) SED decomposition method. We use the AGN templates of Siebenmorgen et al. (2015), because, for a fixed MIR luminosity, their FIR luminosities can reproduce the popular AGN IR SEDs (see Figure 2).

This paper is laid out as follows. In Section 2, we describe our sample and data. In Section 3, we introduce our decomposition method. In Section 4, we show our new AGN FIR SEDs and discuss our results. Conclusions are drawn in Section 5. Throughout this work, we adopt a flat Λ CDM cosmology of $H_0 = 70 \text{ km s}^{-1} \text{ Mpc}^{-1}$ and $\Omega_M = 0.3$ (Peebles & Ratra 2003).

2. SAMPLE AND DATA

Our goal is to verify the result of S16. Therefore, we also adopt the PG quasar sample. Our parent sample includes all 87 objects of the PG quasar sample (e.g., Schmidt & Green 1983; Boroson & Green 1992) at redshift $z < 0.5$ (see Figure 1). We collect the multi-band photometric data as follows: Palomar *B*-band photometry (e.g., Schmidt & Green

¹ For more details about IRS, please refer to <http://irsa.ipac.caltech.edu/data/SPITZER/docs/irs/>.

Table 1. Adopted parameter space of the [Siebenmorgen et al. \(2015\)](#) AGN template library

θ (degree)	19, 33, 43, 52, 60, 67
R_s (10^{15} cm)	300, 514, 772, 1000, 1545
V_c (%)	1.5, 7.7, 38.5, 77.7
A_c	0, 4.5, 13.5, 45
A_d	0, 30, 100, 300, 1000

NOTE— θ , V_c , A_c , and A_d represent the viewing angle, the cloud volume filling factor, the optical depth of an individual cloud, and the optical depth of the disk mid-plane, respectively. R_s corresponds to the inner radius of the dusty torus if an AGN luminosity with $L_{\text{bol}} = 10^{11} L_{\odot}$, where L_{\odot} is the solar luminosity. That is, larger R_s indicates colder dust sublimation temperature (see texts).

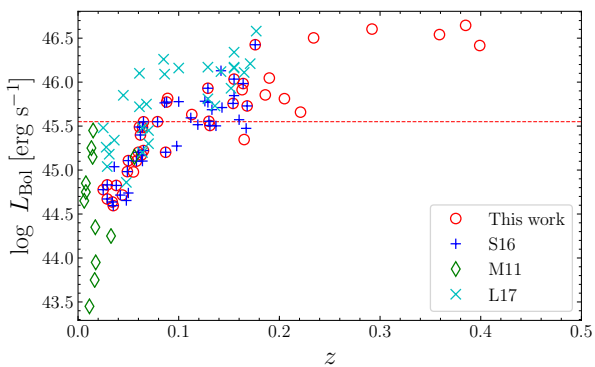


Figure 1. The bolometric luminosity as a function of redshift for our selected PG quasars (42 sources; red open circles), the red dashed line represents the median bolometric luminosity of our sample. For comparison, we also include the AGN samples of S16 (47 sources; blue pluses), M11 (12 sources; green diamonds), and L17 (29 sources; cyan crosses).

1983; Shi et al. 2014), SDSS magnitudes from the SDSS Photometric Catalog (Release 9; Ahn et al. 2012), WISE magnitudes from the AllWISE Source Catalog (Wright et al. 2010), Spitzer/MIPS data from Shi et al. (2014), and the *Herschel*/SPIRE (Griffin et al. 2010) data from Petric et al. (2015). Unlike S16, we exclude the photometric data from 2MASS, ISO and *AKARI*. These data are out of date compared with *Spitzer* and *Herschel* data. We also collect the high-quality *Spitzer* IRS spectra for the 87 quasars from Shi et al. (2014). The spectra are re-binned into $2\mu\text{m}$ intervals, starting from $5.7\mu\text{m}$. The re-binned² data can provide observed-frame 6-30 μm SEDs and are used in the subsequent SED decomposition.

² By re-binning the spectra, the effects of emission/absorption lines on the subsequent SED decomposition can be diluted.

We removed 16 radio-loud (with radio loudness $R > 10$; see Kellermann et al. 1989) sources to avoid the potential contamination from jets. We also dropped two sources without available radio loudness estimates. For the remaining 69 radio-quiet PG quasars, we rejected 23 sources without observations at rest-frame wavelength $\lambda_{\text{rest}} > 200\mu\text{m}$. Thus, the sample for our subsequent analysis consists of 46 quasars. Following S16, we interpolate between the SDSS *ugriz* bands or between the Palomar B-band and 2MASS J-band (in the cases of no SDSS counterparts) to derive the rest-frame 5100 \AA luminosity (i.e., λL_{λ} at 5100 \AA , hereafter L_{5100}). A comparison between the optical-derived and IR-derived rest-frame 5100 \AA luminosities is discussed in the appendix Section A.

The distribution of our sample in the $L_{\text{bol}}-z$ plane is presented in Figure 1. L_{bol} is estimated from L_{5100} with a bolometric factor of 10 (Richards et al. 2006). For comparison purpose, we also show the distributions of samples used in previous works in Figure 1. For each source in the S16 sample, L_{bol} is also estimated from L_{5100} . The AGN IR SED of L17 is based on the AGN sample of Elvis et al. (1994); for each of these AGNs, Elvis et al. (1994) integrated the observed SEDs to derive L_{bol} (see their section 6.1 for details). For AGNs in the M11 sample, we use the hard X-ray luminosity $L_{2-10\text{keV}}$ and the bolometric correction of Lusso et al. (2012) to estimate L_{bol} . The M11 AGNs are less luminous than those of our sample, S16 and L17.

3. SPECTRAL ENERGY DISTRIBUTION DECOMPOSITION

At FIR bands, the galaxy contribution is significant. To isolate the AGN component, we use a two-component SED decomposition. That is, the observed fluxes are

$$f_{\text{obs}} = c_1 f_{\text{AGN}} + c_2 f_{\text{Gal}}, \quad (1)$$

where f_{AGN} and f_{Gal} are the AGN and galaxy fluxes, respectively. The remaining two free parameters are the normalizations of the two templates (i.e., c_1 and c_2).³ It is worth noting that, for each source, the best-fitting galaxy component cannot exceed the observed SED; however, this is not the case in S16. The disadvantage of this method is that we need to use the shapes of known AGN SEDs as a prior. Therefore, we wish to use an AGN template library that covers a wide range of the AGN parameter space and also contains commonly used AGN IR SEDs (e.g., the SEDs of Mullaney et al. 2011; Symeonidis et al. 2016; Lyu & Rieke 2017).

Our AGN templates are selected from Siebenmorgen et al. (2015).⁴ They derived this template library by assuming that the dust clouds near an AGN are distributed in a torus-like

³ With the inclusion of the two free parameters in the galaxy modified blackbody function (i.e., the temperature and power index of frequency) and the five free parameters in Siebenmorgen et al. (2015) AGN template library, the total number of free parameters in our SED fitting is nine.

⁴ For more details about the Siebenmorgen et al. (2015) SED library of AGN torus models, please refer to http://www.eso.org/~rsiebenm/agn_models/index.html.

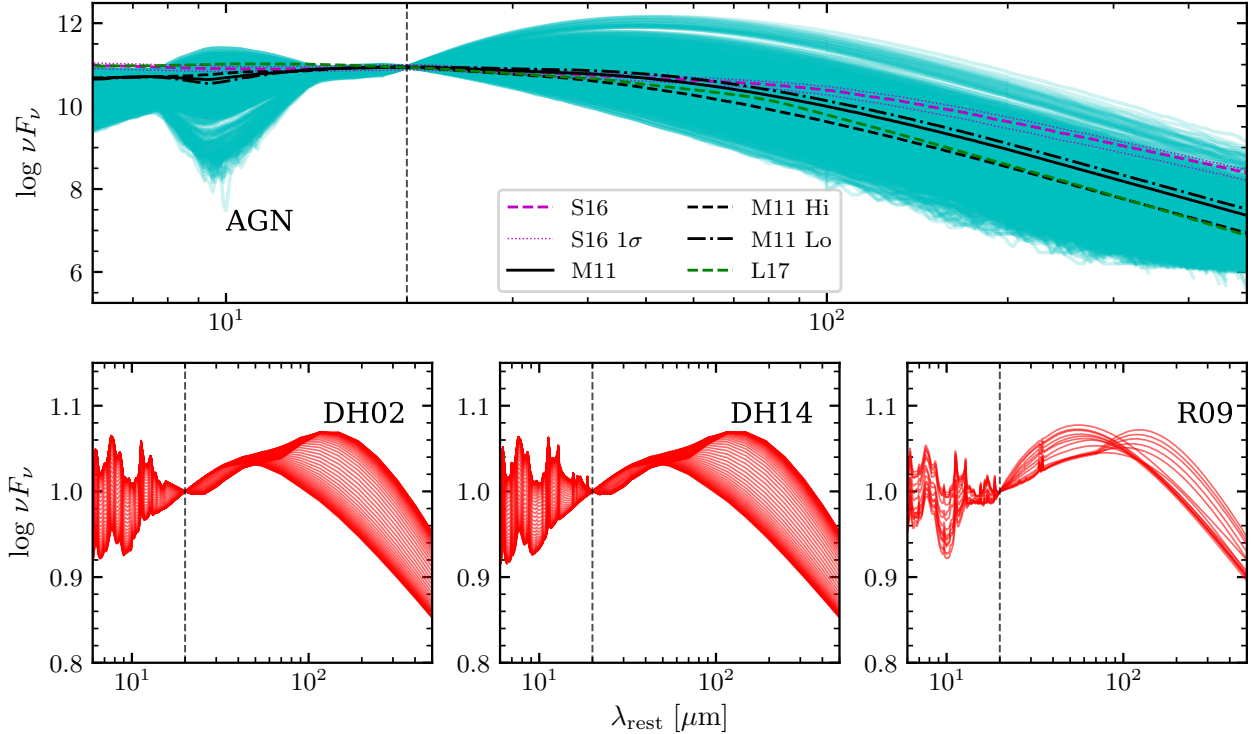


Figure 2. The templates adopted in our SED decomposition. Upper panel: The Siebenmorgen et al. (2015) AGN SED templates (thin cyan curves) and three previous AGN median SEDs (see the legend; the 1σ errors of the S16 SED, mean SEDs of the high-luminosity and low-luminosity subsamples of M11 are also included). Lower panels: three galaxy template libraries from DH02, DH14, and R09, respectively. All the templates are normalized at $20 \mu\text{m}$ (i.e., the vertical dashed lines).

geometry, which may be described by a clumpy medium, a homogeneous disk, or a combination of the two. They considered the AGN dust structure to be approximated by an isothermal disk that is embedded in a clumpy medium. The parameters of this library are θ , V_c , A_c , and A_d (see Table 1 for our adopted parameter space), which represent the viewing angle (in degrees) measured from the pole (z -axis), the cloud volume filling factor, the V -band optical depth of an individual cloud, and the V -band optical depth of the disk mid-plane, respectively. We do not consider templates with the viewing angle $\theta = 73, 80, 86$ since our sources are type-1 AGNs. The remaining free parameter is R_s , which is the inner radius of the dusty torus (in units of 10^{15} cm) for an AGN with fixed bolometric luminosity (i.e., $10^{11} L_\odot$; see Siebenmorgen et al. 2015); that is, R_s indicates the dust sublimation temperature (for more details, see Section 4.2). The templates we select can encompass commonly-used AGN SEDs (see the upper panel of Figure 2).

To test the likely dependency of our results on the choice of galaxy templates, here we consider three galaxy libraries: DH02, DH14, and R09 (see the lower panels of Figure 2). We use SEABASS (Rovilos et al. 2014),⁵ a bayesian SED-

decomposition code, to fit Eq. 1 to the multi-band data. For each source, this code calculates the corresponding “local” maximum likelihoods of all possible combinations of AGN and galaxy templates by varying the normalization factors c_1 and c_2 (via a Monte Carlo Markov Chain sampling algorithm). As a second step, the “local” maximum likelihoods of all possible combinations of templates are compared to determine the “global” maximum value. The template combination (and the best-fitting c_1 and c_2) that gives the “global” maximum likelihood is selected as the best-fitting one. During our SED decomposition, we do not consider any priors. For each source, we record the reduced chi-squared χ_ν^2 of the best-fitting result (see Table 2), and pure AGN model fitted result as a comparison.

Two examples of our SED decomposition results are presented in Figure 3. **Fig. Set 1. displays the two-component SED decomposition results for all our 42 sources.** For comparison, the best-fitting results with the AGN templates alone (i.e., by fixing c_2 in Eq. 1 to be zero) are shown in Figure 14 (and Figset 2), which indicate that a galaxy component is almost always indispensable (also see Table 2 and the appendix Section B).

We visually inspect our fits and find that most of the fits are reasonable, with one example shown in the left panel of Figure 3 (for this fit, the reduced chi-squared $\chi_\nu^2 = 3.028$, also indicating that the goodness-of-fit is acceptable). How-

⁵ For more details about SEABASS, please refer to <http://xraygroup.astro.noa.gr/SEABASS>.

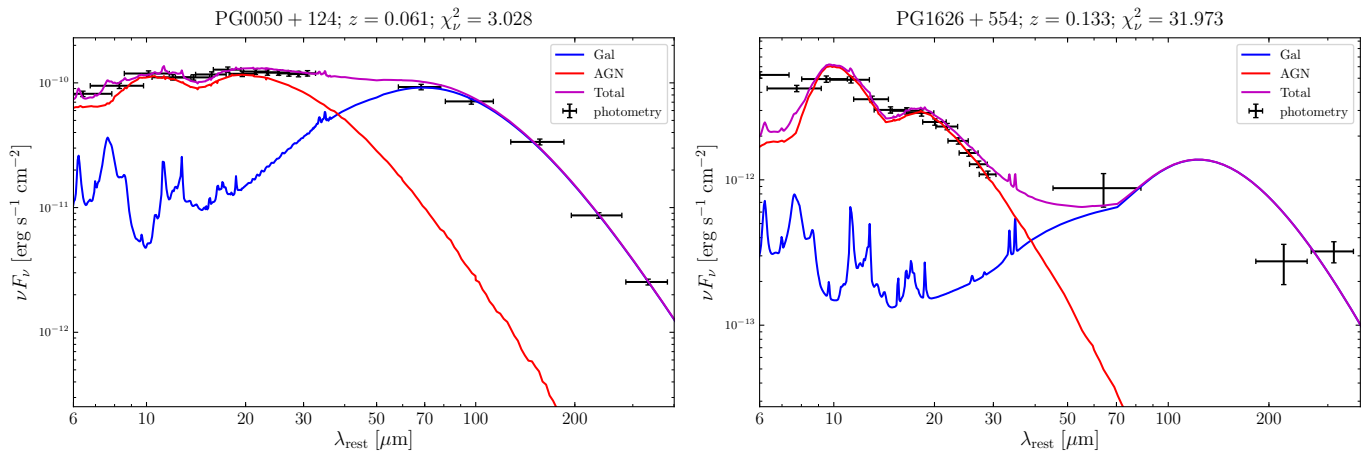


Figure 3. An illustration of our SED decomposition results using the R09 templates. PG0050+124 is an example of reliably fitted sources. The profile matches well to the observed SED. PG1626+554 is an example of unreliably fitted sources, whose best-fit profile does not match the low-quality SED data points. Meanwhile, its observations have limited coverage at $\lambda > 200 \mu\text{m}$. The complete figure set (42 images) is available in the online journal.

Table 2. Reduced χ^2 of our best fitting results.

Name	χ^2_{ν} (AGN+Gal)	χ^2_{ν} (AGN only)
PG0003+199	38.37	2363.87
PG0043+039	5.41	446.13
PG0050+124	3.03	2273.21
PG0052+251	14.62	511.47
PG0157+001	4.58	2728.24
PG0838+770	4.55	650.90
PG2130+099	4.29	846.77
⋮	⋮	
PG2214+139	18.36	9694.58

NOTE—The full table can be seen in the online version.

ever, for four sources, the fits may not be reliable. One such example is shown in the right panel of Figure 3. For PG1626+554, the FIR data are of low quality and not well-sampled, with only two data points at wavelength $> 100 \mu\text{m}$. Therefore, it is quite difficult to determine the FIR profile for this source. Meanwhile, the reduced chi-squared χ^2_{ν} is 31.973 which also indicates that the fit is poor. We reject all these four sources. Therefore, our final sample for subsequent analysis consists of 42 PG quasars. For the 42 sources, the 25-th, 50-th and 75-th percentiles of the distribution of χ^2_{ν} are 2.55, 3.30 and 4.65, respectively. Six sources have $\chi^2_{\nu} > 10$ because the best-fitting models cannot fit the emission around $6 \mu\text{m}$ well. Therefore, we can keep these six sources since we focus on the AGN SED at much longer wavelengths.

4. RESULTS AND DISCUSSION

4.1. Intrinsic AGN IR SED

We can now derive the median AGN IR SED from our best-fitting results. Lani et al. (2017) highlighted that it is important to normalize the individual SEDs to properly account for a small number of very FIR-luminous quasars before calculating the median SED. In contrast, S16 directly calculated the average AGN IR SED without normalizing the individual SEDs. We construct our median SEDs following these two different procedures and find that the two median SEDs are quite similar. We also compare the median SED of all the 27 rejected sources with that of our final sample (Figure 4), finding that the median SEDs are consistent with each other within uncertainties. In our subsequent analysis, we obtain the median SED by first normalizing the individual SEDs to the $40 \mu\text{m}$ luminosity⁶ of the S16 AGN mean SED and only considering the final sample. To assess the differences between two SEDs, we introduce the chi-squared $\chi^2 = \sum \frac{(L_1 - L_2)^2}{dL_1^2 + dL_2^2}$ and far-IR luminosity difference $\Delta \log L = \text{median}\{|\log L_1(\lambda > 100 \mu\text{m}) - \log L_2(\lambda > 100 \mu\text{m})|\}$ as the indicators, where L_1 (L_2) and dL_1 (dL_2) represent the νL_{ν} values of the first (second) SED and the corresponding 1σ uncertainties, respectively. To quantify the SED shape, we define an IR Color Index (hereafter IRCI) as follows. First, we shift the SEDs into the observed frame by using $z = 0.088$ (i.e., the median redshift of our sample); second, we calculate the median values of L_{ν} in the wavelength ranges of $[19.89 \mu\text{m}, 30.94 \mu\text{m}]$ (corresponding to the the MIPS $24 \mu\text{m}$ band on *Spitzer*; hereafter L_{24}) and $[196.54 \mu\text{m}, 298.13 \mu\text{m}]$ (i.e., the SPIRE $250 \mu\text{m}$ band on *Herschel*; hereafter L_{250}); third, IRCI is defined as $\log(L_{24}/L_{250})$. A larger IRCI indicates a hotter SED and vice versa.

⁶ Our conclusions would remain unchanged if we choose to normalize all SEDs to the $20 \mu\text{m}$ luminosity of the S16 AGN mean SED.

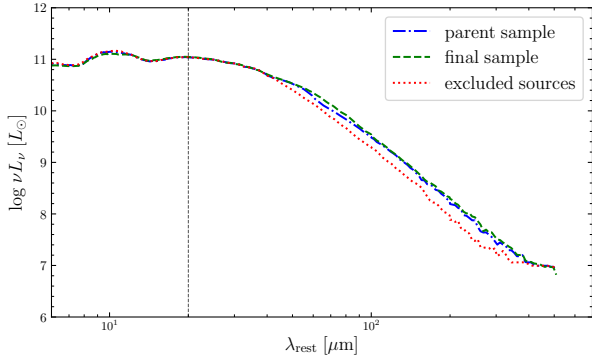


Figure 4. The comparison between the median SED of our final sample and that of the rejected sources. The median SED of the parent sample is also presented. The three median SEDs are consistent with each other within uncertainties (not shown for clarity).

We then explore the dependence of the derived median SED upon the galaxy template library. To do so, we calculate the median SED using each of the three galaxy template libraries (Dale & Helou 2002; Dale et al. 2014; Rieke et al. 2009); the results are presented in Figure 5. It is evident that the median SED of DH02 and that of DH14 are almost the same. The median SED of R09 and that of DH14 are consistent within 2σ uncertainties, with a reduced chi-squared $\chi^2_\nu = 0.86$ and $\Delta \log L = 0.22$ dex; the difference between the IRCI (i.e., ΔIRCI) of the median SED of R09 (IRCI=3.95 dex) and that of DH14 (IRCI=3.56 dex) is 0.39 dex. These differences can be regarded as the intrinsic difference due to different galaxy templates used. When comparing with previous works, we may choose any of the three SEDs as long as the intrinsic difference, $\Delta \text{IRCI} = 0.39$ dex, is taken into account. The median SED using the R09 template library and its 1σ uncertainty is presented in Table 3. In subsequent sections, we focus on the median AGN SED derived using the R09 galaxy template library.

4.2. The IR SED as a function of AGN luminosity

We now compare our median AGN SED with previous works (Figure 6). The IRCIs for our result and previous works are shown in the right panel of Figure 6. Our AGN median IR SED is only slightly hotter than that of L17 with $\Delta \text{IRCI} = 0.47$ dex (i.e., close to the intrinsic scatter due to using different galaxy templates). Our median AGN SED is also somewhat hotter than that of M11 (with $\Delta \text{IRCI} = 0.80$ dex, and $\Delta \log L = 0.57$ dex). The AGNs adopted by M11 are less luminous than those of our final sample, since they used moderate-luminosity AGNs with a median bolometric luminosity $L_{\text{bol}} = 10^{44.05}$ erg s $^{-1}$ calculated using the Lusso et al. (2012) bolometric-correction relation, in contrast to our PG quasars with a median $L_{\text{bol}} = 10^{45.55}$ erg s $^{-1}$. It is worth noting that our median AGN IR SED is close to the M11 high-luminosity AGN median SED (i.e., $\Delta \text{IRCI} = 0.40$ dex and $\delta = 0.30$ dex.) Therefore, we speculate that the differences between our median AGN SED and that of M11 are caused by two factors: first, the AGN IR SED of more

luminous AGNs is hotter than that of the less luminous ones; and second, the data of M11 have limited FIR coverage and their SED is biased (see Section 4.2).

To test our speculations of the differences between our median AGN SED and that of M11, we explore the IR SED as a function of AGN luminosity. We split the final sample into two subsamples, each containing 21 sources: the high-luminosity (i.e., $L_{5100} \geq \tilde{L}_{5100}$, where $\tilde{L}_{5100} = 10^{44.55}$ erg s $^{-1}$ is the median L_{5100} of our full sample) subsample with a median $L_{5100} = 10^{44.91}$ erg s $^{-1}$ and the low-luminosity subsample ($L_{5100} < \tilde{L}_{5100}$) with a median $L_{5100} = 10^{44.11}$ erg s $^{-1}$. We construct the median SEDs for the two subsamples (Figure 7) and find that the high-luminosity subsample (IRCI=3.38 dex) tends to have a cooler median SED (i.e., having systematically higher FIR emission and a smaller IRCI) than the low-luminosity subsample (IRCI=4.58 dex; therefore, $\Delta \text{IRCI} = 1.20$ dex). The median L_{bol} of L17 is $10^{45.85}$ erg s $^{-1}$, which is close to that of our high-luminosity one. The AGN IR SED of L17 is also more consistent with that of our high-luminosity subsample ($\Delta \text{IRCI} = 0.10$ dex) than that of our full sample or low-luminosity subsample. The AGN IR SED of M11 which is obtained from much less luminous AGNs is cooler (i.e., smaller IRCI) than our results. In addition, M11 found that low-luminosity AGNs tend to have cooler SEDs than high-luminosity AGNs (with $\Delta \text{IRCI} = -0.52$ dex), which is inconsistent with the tendency of our results. This inconsistency might be caused by the limited FIR coverage in M11. M11 used the IRAS photometric data that only reach the observed-frame wavelength of 100 μm . They adopted a modified blackbody shape of AGN SED at FIR bands, but there were only two FIR data points (i.e., 60 and 100 μm fluxes, most of which are upper limits) to constrain their SED decomposition. Whereas, we have at least 4 *Spitzer/Herschel* FIR data points (i.e., 60, 100, 160, and 250 μm fluxes) to define our AGN IR SEDs.

The dependence of AGN IR SED on luminosity might be caused by the change of torus properties. To look into this, we collect the best-fitting torus parameters from our SED decomposition. In Figure 8, we compare the distributions of each parameter between the low-/high-luminosity samples.⁷ We find that high-luminosity AGNs tend to have larger mid-plane optical depths and smaller cloud filling factors than low-luminosity ones (see Figure 8; indeed, in each panel, the Anderson-Darling test indicates that, at the 99% significance level or above, the null hypothesis that the two distributions

⁷ To demonstrate the uncertainties of the best-fitting parameters, we choose three representative sources whose luminosities correspond to the 25th, 50th, and 75th percentile luminosity in our sample to represent the low-/median-/high-luminosity sources. First, we create 128 mock SEDs for each of the three sources by adding Gaussian noise to the observed SEDs. For each source, we then fit mock SEDs following the same methodology and obtain the distributions of the torus parameters. We report the differences between the 16th and 84th percentiles of each distribution as the error bar for each parameter (i.e., the horizontal lines in each panel of Figure 8).

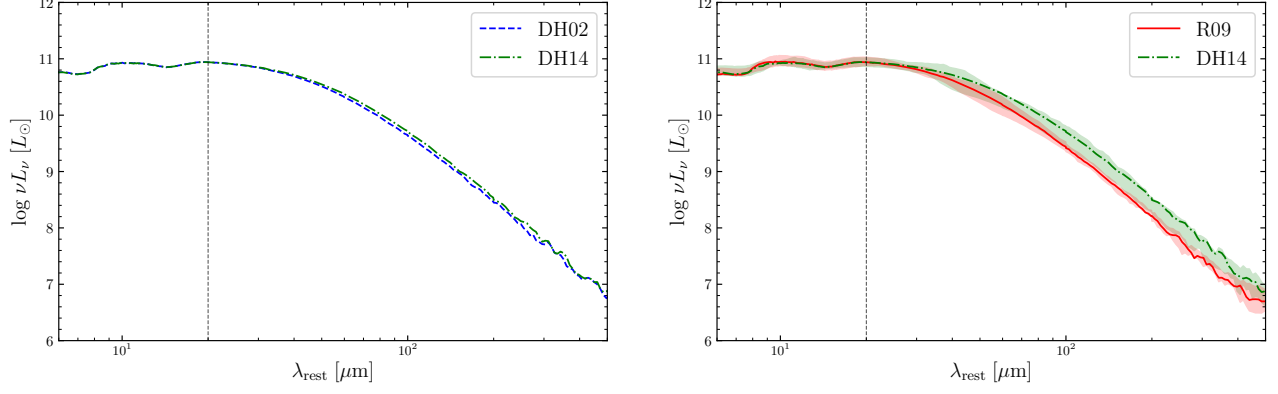


Figure 5. The dependence of our median AGN SEDs upon the choice of galaxy templates. Left panel: the median SED derived with the DH02 galaxy template library versus that with DH14. Right panel: the median SED derived with DH14 versus that with R09. The shaded regions indicate the interquartile ranges (i.e., between the 25th and 75th percentiles) that are estimated via bootstrapping. The three median SEDs are consistent with each other (within 2σ uncertainties), with $\chi^2_{\nu} = 0.86$ and $\delta = 0.22$ dex between the DH14 and R09 results. The difference in IRC1 is 0.39 dex.

Table 3. Our AGN median SEDs

Wavelength	All-Median	All-upper	All-lower	hi-Median	hi-upper	hi-lower	lo-Median	lo-upper	lo-lower
μm	$\log(L_{\odot})$	$\log(L_{\odot})$	$\log(L_{\odot})$	$\log(L_{\odot})$	$\log(L_{\odot})$	$\log(L_{\odot})$	$\log(L_{\odot})$	$\log(L_{\odot})$	$\log(L_{\odot})$
(1)	(2)	(3)	(4)	(5)	(6)	(7)	(8)	(9)	(10)
6.0	10.72	10.838	10.691	10.812	10.847	10.634	10.67	10.806	10.558
6.1	10.726	10.846	10.695	10.808	10.837	10.62	10.671	10.803	10.566
6.2	10.726	10.846	10.703	10.811	10.848	10.638	10.675	10.806	10.56
6.3	10.736	10.858	10.703	10.813	10.848	10.638	10.674	10.807	10.555
6.4	10.729	10.853	10.705	10.804	10.838	10.627	10.681	10.798	10.585
6.6	10.725	10.859	10.704	10.806	10.85	10.627	10.685	10.798	10.593
6.8	10.716	10.856	10.703	10.8	10.845	10.617	10.692	10.788	10.6
6.9	10.72	10.857	10.703	10.797	10.843	10.626	10.687	10.79	10.61
7.0	10.717	10.856	10.703	10.788	10.823	10.622	10.689	10.783	10.598
7.1	10.719	10.858	10.709	10.797	10.839	10.617	10.7	10.792	10.637
7.3	10.72	10.861	10.712	10.789	10.834	10.625	10.704	10.784	10.637
7.5	10.73	10.865	10.729	10.791	10.831	10.617	10.717	10.786	10.662
7.6	10.741	10.866	10.736	10.8	10.848	10.636	10.718	10.795	10.652
7.7	10.756	10.877	10.741	10.812	10.859	10.658	10.736	10.811	10.674
7.8	10.774	10.884	10.743	10.819	10.858	10.663	10.733	10.815	10.657
7.9	10.808	10.895	10.761	10.843	10.886	10.697	10.747	10.837	10.682
8.0	10.833	10.907	10.772	10.866	10.892	10.719	10.767	10.856	10.707
8.2	10.868	10.932	10.79	10.905	10.916	10.769	10.787	10.88	10.728
8.4	10.901	10.965	10.802	10.923	10.936	10.809	10.81	10.902	10.758
8.5	10.908	10.984	10.805	10.935	10.953	10.826	10.816	10.907	10.767

NOTE—(1) Wavelength; (2)–(10) $\log \nu L_{\nu}$ of our AGN SEDs; “hi-Median” and “lo-Median” refer to the median SEDs of the $\log L_{5100} > 44.55$ and the $\log L_{5100} < 44.55$ subsamples, respectively; “-upper” and “-lower” postfixes refer to the 75th- and 25th-percentile SEDs for each sample, which are derived by bootstrapping. The SEDs are normalized to the S16 average AGN SED at 40 μm . The full table is published in its entirety in the machine-readable format. A portion is shown here for guidance purpose.

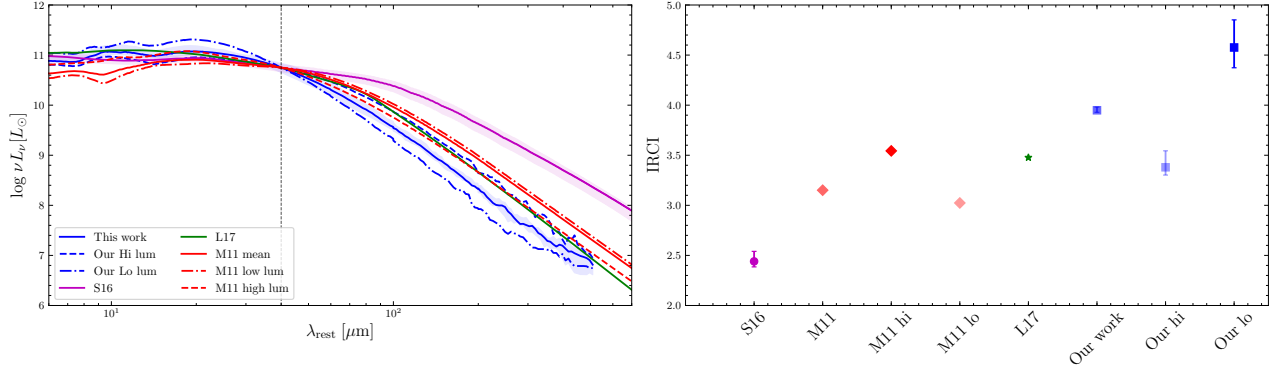


Figure 6. A comparison between our results and previous works. The blue solid curve represents the median AGN IR SEDs of our full sample. And the pink, green, and red curves are from S16, L17, and M11. The dashed and dash-dotted curves indicate the median AGN SEDs of high- and low-luminosity sample in this work, respectively. Our median AGN IR SED is roughly consistent with that of L17 and the M11 high-luminosity AGNs within uncertainties, but significantly disagree with that of S16. The shaded regions represent available 1σ uncertainties (derived via bootstrapping).

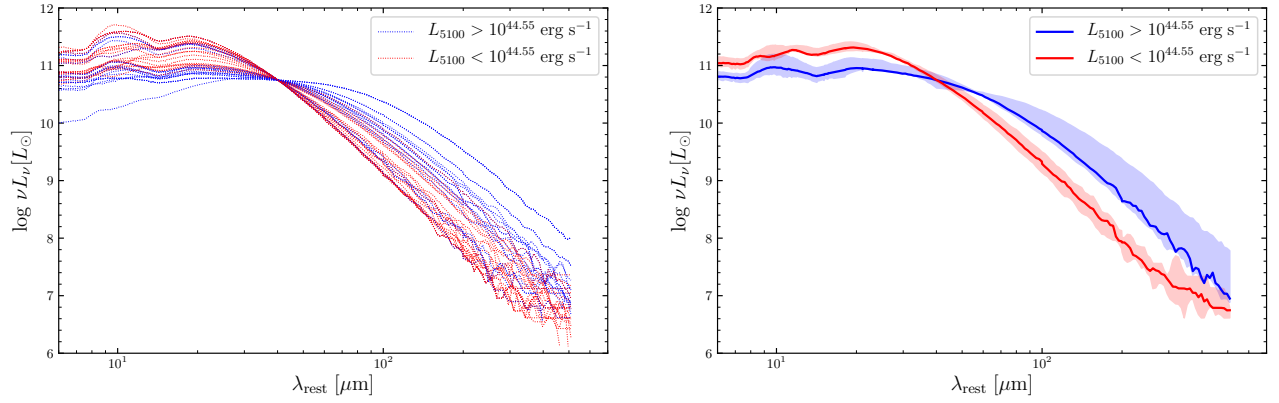


Figure 7. The AGN SEDs for our high- and low-luminosity subsamples. Left panel: Blue (red) dotted curves represent AGN SEDs of sources with L_{5100} greater (less) than the median L_{5100} ($10^{44.55} \text{ erg s}^{-1}$). Right panel: The blue and red solid curves represent the median SEDs of the high- and low-luminosity AGN subsamples, respectively. Shaded regions are the 1σ uncertainties derived by bootstrapping. Luminous sources tend to have cooler SEDs (i.e., larger FIR fluxes for fixed MIR emission) than less luminous ones.

are the same can be rejected). It is also clear in the right panel that luminous AGNs have tori of larger inner radii R_S .

In the torus model of [Siebenmorgen et al. \(2015, see their Section 2.2\)](#), the AGN luminosity is fixed to be $10^{11}L_\odot$ and R_S is allowed to vary. Then, to understand the meaning of R_S , let us consider a dusty torus model with fixed dust composition whose geometric distribution is sublimation-radius-scale-invariant. The only variable parameters are the dust sublimation radius r_{sub} (which is not R_S) and the AGN luminosity (L_{AGN}). The AGN flux F_{AGN} received at the sublimation radius, i.e., $F_{\text{AGN}} = L_{\text{AGN}}/(4\pi r_{\text{sub}}^2)$, should equal the flux of the re-emitted infrared blackbody emission (i.e., σT_{sub}^4 , where σ and T_{sub} are the Stefan-Boltzmann constant and the dust sublimation temperature, respectively) under the assumption of steady state. Therefore, it is evident that

$$r_{\text{sub}} = R_S \sqrt{L_{\text{AGN},0}/L_{\text{AGN}}}, \quad (2)$$

where $R_S = (L_{\text{AGN},0}/(4\pi\sigma T_{\text{sub}}^4))^{0.5}$ is the sublimation radius for an AGN with $L_{\text{AGN},0} = 10^{11}L_\odot$ whose torus dust sublimation temperature is identical to the AGN with L_{AGN} . That is, the $L_{\text{AGN}} \propto r_{\text{d}}^2$ relation (which has been observed; see, e.g., [Kishimoto et al. 2011](#)) adopted by [Siebenmorgen et al. \(2015\)](#) ensures that an AGN with L_{AGN} and r_{sub} shares the same dust sublimation temperature with another AGN with $L_{\text{AGN},0}$ and R_S . Then, the two AGNs have the same torus SED shape.⁸ We expect that, since [Siebenmorgen et al. \(2015\)](#) fixed the AGN luminosity to be $L_{\text{AGN},0} = 10^{11}L_\odot$, $R_S \propto T_{\text{sub}}^{-2}$, i.e., R_S actually indicates the dust sublimation temperature (as indicated in Figure 8 (c)). Therefore, our result that luminous AGNs tend to have larger R_S suggests that higher-luminosity AGNs tend to have lower dust sublimation temperatures.

It should be noted that the torus model of [Siebenmorgen et al. \(2015\)](#) is a phenomenological model. The physical reasons for the differences between the IR SEDs of the high- and low-luminosity subsamples can be very complicated. We suspect that, compared with the low-luminosity subsample, AGNs in the high-luminosity subsample might have smaller covering factors (see panel (a) of Figure 8; possibly because more luminous AGNs can more effectively swipe gas and dust away than the less luminous ones) and the UV/optical photons from the central engine can heat the dust on the galaxy scale ([Sanders et al. 1989](#)); these dust clouds are presumably colder than the dusty torus. As a result, the IR SED of the high-luminosity subsample is cooler than the low-luminosity one. Moreover, the high-luminosity sources presumably harbor more massive supermassive black holes than the low-luminosity counterparts. Then, it is natural to expect that the host galaxies of the high-luminosity sources are also more massive and have higher metallicity than those of the low-luminosity ones. The difference in metallicity might also be responsible for the differences in IR SEDs (e.g., [En-](#)

[gelbracht et al. 2008](#)). A detail investigation of the physical mechanisms that are responsible for the IR SED differences is beyond the scope of this work.

M11 argued that higher-luminosity AGNs can heat a larger fraction of their surrounding dust to higher temperatures and they tend to produce a warmer SED (i.e., having stronger emission at MIR wavelengths). In this work, we show that higher-luminosity AGNs tend to have lower dust temperatures. Therefore, higher-luminosity AGNs tend to show more FIR emission with respect to MIR emission and have smaller IR color indices (see also Section 3 and Figure 5 of [Siebenmorgen et al. 2015](#)). Therefore, as the AGN luminosity increases, the SED becomes cooler.

It should be noted that the AGN IR SED of S16 is luminosity-independent (see Figure 6 of S16). The lack of luminosity-dependency might indicate that the stellar contribution is not well subtracted from the total SED (see Section 4.3 for more discussions).

4.3. Reliability of PAH relating to galaxy infrared properties

S16 used PAH fluxes and the DH02 galaxy template library to determine the stellar contribution to the total SED. However, the PAH features can be easily contaminated by the nearby Silicate absorption. To verify the reliability of using the $11.3 \mu\text{m}$ PAH strength as an indicator of the FIR emission due to star formation, we check the PAH fluxes of our best-fitting models for the three galaxy libraries by adopting the following methodology for the S16 sample.⁹ First, we simulate mock IRS spectra according to our best-fitting AGN and galaxy templates. During the simulation, we ensure that the mock spectra and the observed IRS spectra have the same wavelength resolution and suffer from the same measurement errors. We then fit both the mock spectra and the observed IRS data following the same methodology of [Shi et al. \(2007\)](#). We choose to fit the observed IRS data rather than use the result of [Shi et al. \(2007\)](#) because the observed IRS data have been re-calibrated and re-processed since [Shi et al. \(2007\)](#). To estimate the measurement uncertainties on PAH fluxes, we adopt a Monte Carlo approach by adding Gaussian flux-density noise (with a standard deviation being the measurement error) to the flux in each bin of wavelength and generating a new spectrum. We then refit the new spectrum following the same methodology. For each source, this procedure is repeated 1000 times to obtain the distribution of the PAH flux; the measurement uncertainties are then estimated as the 25th- and 75th- percentiles of the PAH flux distribution. For some sources, the 25th percentiles are smaller than zero; we report the 90th percentiles as the upper limits. A comparison between our measurements of the IRS data and those of [Shi et al. \(2007\)](#) is illustrated in Figure 9. Overall, we find no significant systematic offset between the two sets

⁸ This is why the AGN luminosity is fixed to be $10^{11}L_\odot$ in [Siebenmorgen et al. \(2015, see their Section 2.2\)](#).

⁹ All but one S16 sources are also in our parent sample. Therefore, we can use our SED decomposition method (see Section 3) to find the best-fitting AGN and galaxy templates for the S16 sources.

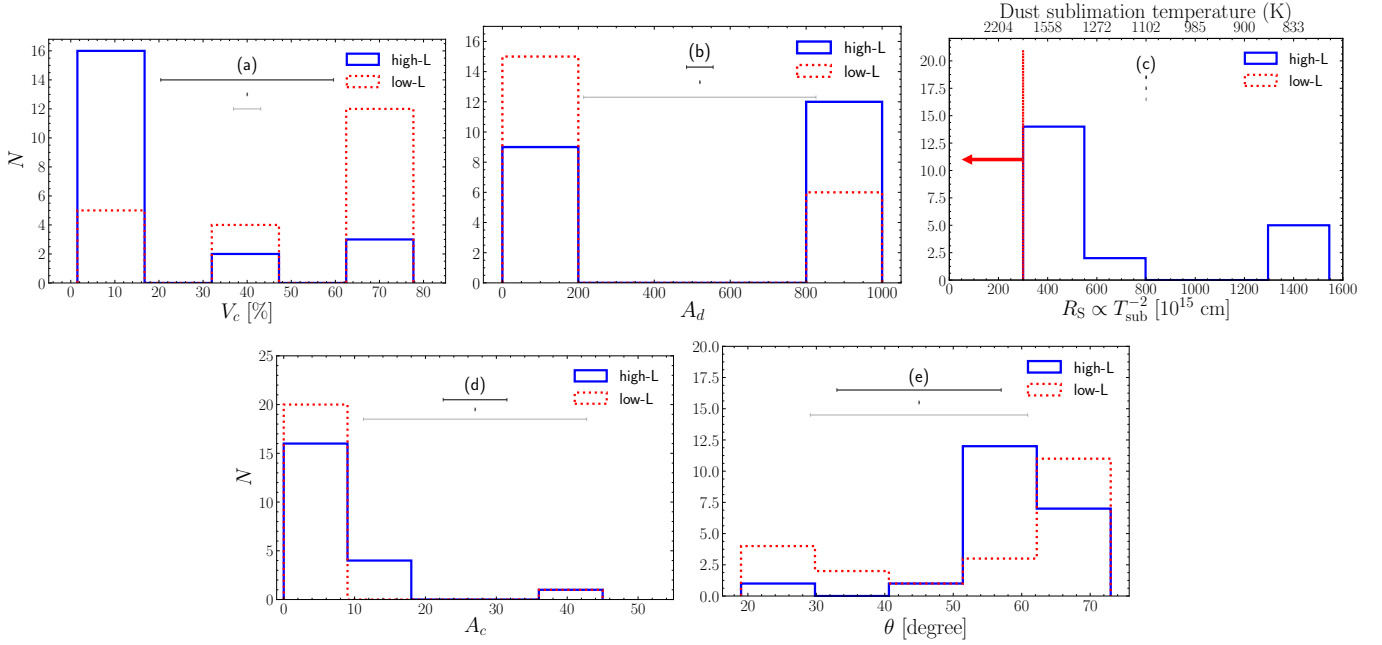


Figure 8. The comparison of the distributions of V_c , A_d , R_s , A_c and θ for the high-luminosity subsample (blue histograms) and low-luminosity subsample (red histograms). The distribution of A_d shows a gap between 200 and 800, which might be caused by the large gap in the parameter space of A_d (see Table 1) in the model of Siebenmorgen et al. (2015). High-luminosity AGNs tend to have larger mid-plane optical depths (A_d), smaller cloud filling factors (V_c), and larger inner radii (R_s ; which indicates colder dust sublimation temperature). Interestingly, the low-luminosity AGNs seem to prefer R_s values that hit the lower bound of the allowed R_s space. The distributions of A_c (or θ) for the two subsamples are statistically indistinguishable given $p > 0.05$ from the Anderson-Darling tests. In each panel, the three horizontal lines from bottom to top show the corresponding error bars of the three representative sources with the 25th-, 50th-, 75th-percentile luminosities in our final sample, respectively. Some parameters have zero error bars; this is because the parameter space of the torus model is too sparse to infer the 1σ errors, i.e., the 1σ errors are smaller than the step sizes of the parameters (see Table 1). The leftward red arrow in panel (c) indicates the trend of R_s for the low-luminosity subsample if the R_s parameter space can reach smaller values.

of measurements albeit with some scatter. This is not surprising given that the fitting method is the same but the data calibration has been updated (Shi et al. 2014). As for sources without the detections of the PAH 11.3μ features, Shi et al. (2007) used the 5σ measurement noise as the upper limits; instead, we report the 90th-percentiles of the Monte Carlo simulations as the upper limits. Therefore, at the low flux end (i.e., $< 3 \times 10^{-14} \text{ erg s}^{-1} \text{ cm}^{-2}$), the results of Shi et al. (2007) are larger than our measurements by (on average) a factor of ~ 2 .

The PAH fluxes of mock spectra for the three galaxy template libraries are presented in Figure 10. It is clear that the PAH fluxes derived using the DH02 and DH14 libraries are systematically larger than those derived with R09. Indeed, the median PAH strength values of DH02 and DH14 are 181% and 165% than those of R09, respectively. This difference is likely a result of contamination by the silicate absorption, which is not accounted for in DH02 or DH14 but taken into account in R09. If the silicate absorption is indeed important, the observed PAH flux would be an underestimation of the true value. In addition, if one estimates the galaxy contribution to the total SED by selecting the DH02 or DH14 template with the PAH flux that is closest to the observed one (e.g., S16), the galaxy contribution would also

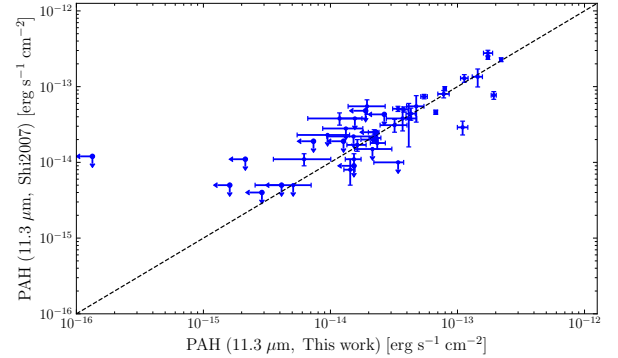


Figure 9. The comparison of $11.3 \mu\text{m}$ PAH flux measurements of the observed IRS data between our work and Shi et al. (2007). Error bars indicate the 25th- and 75th- percentiles; upper limits correspond to the 90th percentiles. The dashed line indicates the one-to-one relation. There is no significant systematic offset between the two sets of measurements.

be underestimated; this is not the case if one adopts the R09 library (see also Figure 3 of Lyu & Rieke 2017). Therefore, using the PAH strength to determine the galaxy contribution to the total SED is highly uncertain and template-dependent.

M11 and our work derive the AGN SED by performing SED decomposition and do not suffer this problem.

The MIR spectra are often dominated by AGN emission. The PAH signal is often very weak and diluted by the silicate absorption feature in an AGN spectrum. Therefore, the PAH flux measurement might be underestimated. To illustrate this possible underestimation, we generate two sets of mock IRS spectra: for each source in our sample, we generate a mock spectrum by only considering the best-fitting R09 template and another mock spectrum by combining the best-fitting R09 and AGN templates (i.e., according to Eq. 1). Then, we measure the PAH fluxes from the two sets of mock spectra (Figure 11). In the presence of AGN contamination, the PAH flux is overall slightly underestimated (i.e., by 20%), and this bias is more evident towards the low PAH flux end.

In Figure 12, we plot the PAH fluxes of the mock IRS spectra (including the AGN component) versus those of the observed IRS data. It is clear that, when using the R09 library, the mock PAH fluxes are generally consistent with observations (also see Lyu & Rieke 2017), while both the DH02 and DH14 libraries tend to over-estimate PAH fluxes. If the PAH emission is not significantly suppressed in AGN hosts and can be used as a good star-formation tracer (see, e.g., Shi et al. 2007; Lutz et al. 2008; Watabe et al. 2008; Rawlings et al. 2013; Esquej et al. 2014; Symeonidis et al. 2016), then our results suggest that the R09 library is more appropriate to PG quasars than the DH02 or DH14 library. On the other hand, if AGN feedback destroys PAH (see, e.g., Aitken & Roche 1985; Voit 1992), it may not be valid to infer the stellar contribution from the PAH emission. Our SED-decomposition results are largely independent of the choice of galaxy library (see Figure 5). Thus our AGN IR SED is more robust than the PAH-based results.

5. CONCLUSIONS

In this work, we revisit the AGN intrinsic IR SED by adopting the SED-decomposition technique. We use the AGN template library of Siebenmorgen et al. (2015) as this library contains previous commonly-used AGN SEDs (e.g., Mullaney et al. 2011; Symeonidis et al. 2016; Lyu & Rieke 2017). We test three galaxy template libraries, i.e., DH02, DH14, and R09. Compared to S16 (47 $z < 0.18$ PG quasars), our final sample (consisting of 42 sources) contains PG quasars extending to higher redshifts ($z < 0.5$); in ad-

dition, unlike the PAH-based method of S16, our intrinsic AGN IR SED proves to be insensitive to the choice of galaxy template library. Furthermore, our fitting results do not have cases where the galaxy component exceeds the observed total SED as seen in S16. Our derived AGN IR SEDs are available in Table 3. The main results of this work are as follows:

- Through SED decomposition, we derive a median AGN IR SED between 6 μm to 500 μm . Our median IR SED is generally consistent with those of M11 and L17, but in contrast to that of S16 (i.e., S16 underestimated the galaxy FIR contribution, and obtained a very cool AGN FIR SED; see Figure 6). We speculate that the stellar contribution was not well determined/subtracted in S16 because they adopted the DH02 galaxy template library and PAH fluxes to determine the stellar contribution.
- We find that the AGN IR SED tends to be cooler (i.e., a higher fraction of FIR emission) with increasing AGN luminosity (Figure 7). This luminosity-dependent SED evolution might be explained if more luminous AGNs tend to have stronger radiative feedback to change torus structures and/or their tori have higher metallicities (see Section 4.2).
- Our results do not depend upon the choice of galaxy template library (see Figure 5). Meanwhile, we find that the conversion of the PAH emission to galaxy SED varies with the choice of galaxy template library (see Figure 10). If the R09 galaxy template library is more appropriate to PG quasar hosts, the PAH fluxes predicted by our best fit models are consistent with those observed (Figure 12).

6. ACKNOWLEDGEMENTS

We thank the anonymous referees for their helpful comments that significantly improved the paper. We thank Yong Shi for providing his PAH fitting code. J.X., M.Y.S., and Y.Q.X. acknowledge the support from the China Postdoctoral Science Foundation (2016M600485), NSFC-11603022, NSFC-11890693, NSFC-11421303, the CAS Frontier Science Key Research Program (QYZDJ-SSW-SLH006), and the K.C. Wong Education Foundation.

REFERENCES

- Ahn, C. P., Alexandroff, R., Allende Prieto, C., et al. 2012, *ApJS*, 203, 21
- Aitken, D. K., & Roche, P. F. 1985, *MNRAS*, 213, 777
- Antonucci, R. 1993, *ARA&A*, 31, 473
- Barvainis, R. 1987, *ApJ*, 320, 537
- Blandford, R. D., & Payne, D. G. 1982, *MNRAS*, 199, 883
- Boroson, T. A., & Green, R. F. 1992, *ApJS*, 80, 109
- Cao, X., & Spruit, H. C. 2013, *ApJ*, 765, 149
- Dale, D. A., Helou, G., Contursi, A., Silbermann, N. A., & Kolhatkar, S. 2001, *ApJ*, 549, 215
- Dale, D. A., & Helou, G. 2002, *ApJ*, 576, 159
- Dale, D. A., Helou, G., Magdis, G. E., et al. 2014, *ApJ*, 784, 83
- Desert, F.-X., Boulanger, F., & Puget, J. L. 1990, *A&A*, 237, 215
- Elvis, M., Wilkes, B. J., McDowell, J. C., et al. 1994, *ApJS*, 95, 1
- Engelbracht, C. W., Rieke, G. H., Gordon, K. D., et al. 2008, *ApJ*, 678, 804

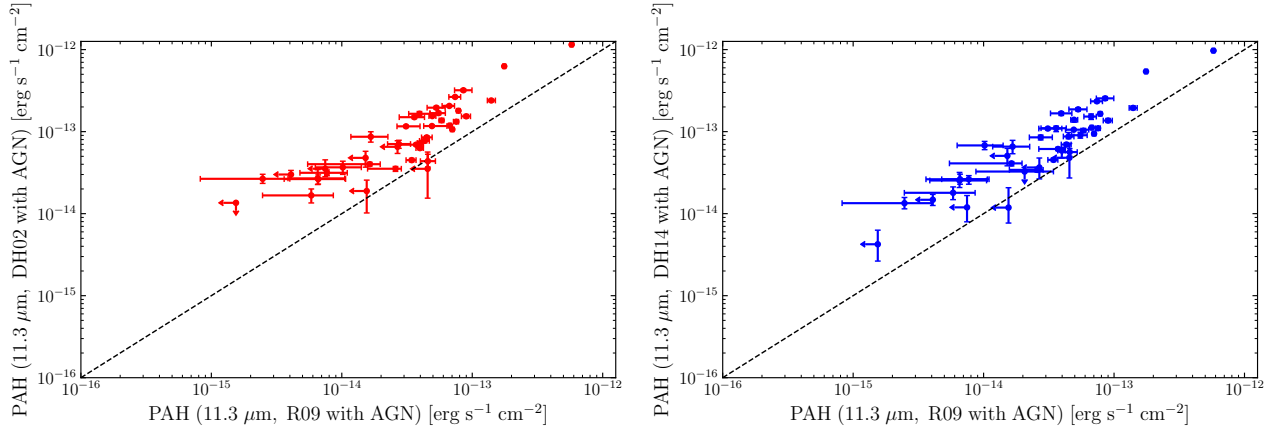


Figure 10. The measurements of $11.3 \mu\text{m}$ PAH fluxes of the mock spectra using different galaxy template libraries. Left panel: The result of DH02 mock spectra versus that of R09 mock spectra. Right panel: The result of DH14 mock spectra versus that of R09 mock spectra. The dashed lines indicate the one-to-one relations. The DH02 and DH14 results are systematically larger than the R09 result. Compared to the R09 result, for the fixed PAH flux measured from real data, the DH02 and DH14 libraries underestimate the galaxy FIR fluxes (see section 4.3).

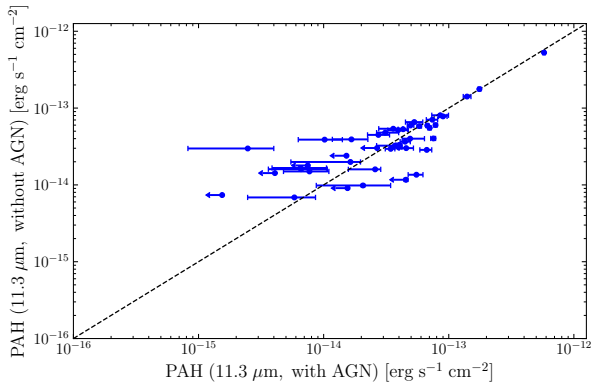


Figure 11. The comparison between $11.3 \mu\text{m}$ PAH flux measurements for R09 mock spectra with and without the AGN component. The dashed line indicates the one-to-one relation. In the presence of AGN contamination, the PAH flux is slightly underestimated. The dispersion can be large when the PAH feature is very weak.

Esquej, P., Alonso-Herrero, A., González-Martín, O., et al. 2014, *ApJ*, 780, 86
 Fabian, A. C. 2012, *ARA&A*, 50, 455
 Ferrarese, L., & Merritt, D. 2000, *ApJL*, 539, L9
 Filiz Ak, N., Brandt, W. N., Hall, P. B., et al. 2014, *ApJ*, 791, 88
 Gebhardt, K., Richstone, D., Kormendy, J., et al. 2000, *AJ*, 119, 1157
 Griffin, M. J., Abergel, A., Abreu, A., et al. 2010, *A&A*, 518, L3
 Grier, C. J., Hall, P. B., Brandt, W. N., et al. 2015, *ApJ*, 806, 111
 Gu, W.-M. 2015, *ApJ*, 799, 71
 Gültekin, K., Richstone, D. O., Gebhardt, K., et al. 2009, *ApJ*, 698, 198
 Häring, N., & Rix, H.-W. 2004, *ApJL*, 604, L89
 Harrison, C. M., Alexander, D. M., Mullaney, J. R., et al. 2012, *ApJL*, 760, L15

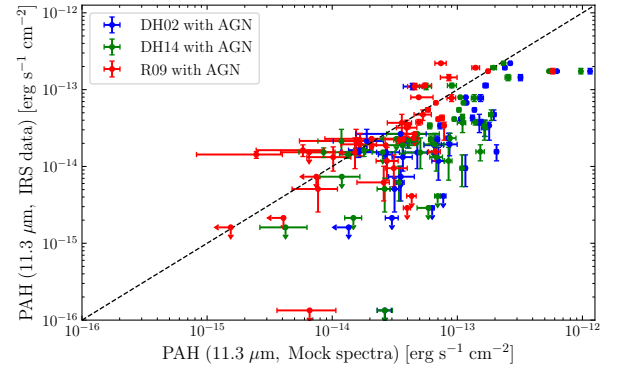


Figure 12. The $11.3 \mu\text{m}$ PAH fluxes of our mock spectra versus those of the observed IRS data. The red, blue, and green dots are for the R09, DH02, and DH14 libraries. The dashed line indicates the one-to-one relation. Among the three galaxy template libraries, the R09 PAH emission is roughly consistent with observations. For the DH02 and DH14 libraries, the PAH emission is over-estimated. This is likely due to the fact that the silicate absorption feature is not properly modeled in these two libraries.

He, Z., Wang, T., Liu, G., et al. 2019, *Nature Astronomy*, 3, 265
 Houck, J. R., Charmandaris, V., Brandl, B. R., et al. 2004, *ApJS*, 154, 211
 Kormendy, J., & Richstone, D. 1992, *ApJ*, 393, 559
 Kormendy, J., & Ho, L. C. 2013, *ARA&A*, 51, 511
 Kishimoto, M., Hönig, S. F., Antonucci, R., et al. 2011, *A&A*, 527, A121
 Kellermann, K. I., Sramek, R., Schmidt, M., Shaffer, D. B., & Green, R. 1989, *AJ*, 98, 1195
 Kennicutt, R. C., Jr. 1998, *ARA&A*, 36, 189
 King, A. 2003, *ApJL*, 596, L27
 Lutz, D., Sturm, E., Tacconi, L. J., et al. 2008, *ApJ*, 684, 853

- Lusso, E., Comastri, A., Simmons, B. D., et al. 2012, *MNRAS*, 425, 623
- Lyu, J., & Rieke, G. H. 2017, *ApJ*, 841, 76
- Lani, C., Netzer, H., & Lutz, D. 2017, *MNRAS*, 471, 59
- Marcillac, D., Rigby, J. R., Rieke, G. H., & Kelly, D. M. 2007, *ApJ*, 654, 825
- Magorrian, J., Tremaine, S., Richstone, D., et al. 1998, *AJ*, 115, 2285
- Marcillac, D., Elbaz, D., Chary, R. R., et al. 2006, *A&A*, 451, 57
- McNamara, B. R., Wise, M., Nulsen, P. E. J., et al. 2000, *ApJL*, 534, L135
- Mullaney, J. R., Alexander, D. M., Goulding, A. D., & Hickox, R. C. 2011, *MNRAS*, 414, 1082
- Murray, N., Chiang, J., Grossman, S. A., & Voit, G. M. 1995, *ApJ*, 451, 498
- Mou, G., Wang, T., & Yang, C. 2017, *ApJ*, 844, 30
- Netzer, H., Lutz, D., Schweitzer, M., et al. 2007, *ApJ*, 666, 806
- Neugebauer, G., Miley, G. K., Soifer, B. T., & Clegg, P. E. 1986, *ApJ*, 308, 815
- Page, M. J., Symeonidis, M., Vieira, J. D., et al. 2012, *Nature*, 485, 213
- Peebles, P. J., & Ratra, B. 2003, *Reviews of Modern Physics*, 75, 559
- Petric, A. O., Ho, L. C., Flagey, N. J. M., & Scoville, N. Z. 2015, *ApJS*, 219, 22
- Proga, D., & Kallman, T. R. 2004, *ApJ*, 616, 688
- Rawlings, J. I., Seymour, N., Page, M. J., et al. 2013, *MNRAS*, 429, 744
- Reynolds, C. S., Ward, M. J., Fabian, A. C., & Celotti, A. 1997, *MNRAS*, 291, 403
- Richards, G. T., Lacy, M., Storrie-Lombardi, L. J., et al. 2006, *ApJS*, 166, 470
- Richards, G. T., Kruczek, N. E., Gallagher, S. C., et al. 2011, *AJ*, 141, 167
- Rigopoulou, D., Spoon, H. W. W., Genzel, R., et al. 1999, *AJ*, 118, 2625
- Rieke, G. H. 1978, *ApJ*, 226, 550
- Richards, G. T., Lacy, M., Storrie-Lombardi, L. J., et al. 2006, *ApJS*, 166, 470
- Rieke, G. H., Alonso-Herrero, A., Weiner, B. J., et al. 2009, *ApJ*, 692, 556
- Rovilos, E., Georgantopoulos, I., Akylas, A., et al. 2014, *MNRAS*, 438, 494
- Sanders, D. B., Phinney, E. S., Neugebauer, G., Soifer, B. T., & Matthews, K. 1989, *ApJ*, 347, 29
- Schmidt, M., & Green, R. F. 1983, *ApJ*, 269, 352
- Shakura, N. I., & Sunyaev, R. A. 1973, *A&A*, 24, 337
- Shi, Y., Ogle, P., Rieke, G. H., et al. 2007, *ApJ*, 669, 841
- Shi, Y., Rieke, G. H., Ogle, P. M., Su, K. Y. L., & Balog, Z. 2014, *ApJS*, 214, 23
- Siebenmorgen, R., Heymann, F., & Efstathiou, A. 2015, *A&A*, 583, A120
- Silk, J., & Rees, M. J. 1998, *A&A*, 331, L1.
- Stanley, F., Harrison, C. M., Alexander, D. M., et al. 2015, *MNRAS*, 453, 591
- Sun, M., Trump, J. R., Brandt, W. N., et al. 2015, *ApJ*, 802, 14
- Sun, M., Xue, Y., Richards, G. T., et al. 2018, *ApJ*, 854, 128
- Sun, M., Xue, Y., Trump, J. R., & Gu, W.-M. 2019, *MNRAS*, 482, 2788
- Symeonidis, M., Giblin, B. M., Page, M. J., et al. 2016, *MNRAS*, 459, 257
- Tombesi, F., Cappi, M., Reeves, J. N., et al. 2013, *MNRAS*, 430, 1102
- Tremaine, S., Gebhardt, K., Bender, R., et al. 2002, *ApJ*, 574, 740
- Tristram, K. R. W., Meisenheimer, K., Jaffe, W., et al. 2007, *A&A*, 474, 837
- Trump, J. R., Hall, P. B., Reichard, T. A., et al. 2006, *ApJS*, 165, 1
- Urry, C. M., & Padovani, P. 1995, *PASP*, 107, 803
- Voit, G. M. 1992, *MNRAS*, 258, 841
- Wright, E. L., Eisenhardt, P. R. M., Mainzer, A. K., et al. 2010, *AJ*, 140, 1868-1881
- Watabe, Y., Kawakatu, N., & Imanishi, M. 2008, *ApJ*, 677, 895
- Yuan, F., Wu, M., & Bu, D. 2012a, *ApJ*, 761, 129

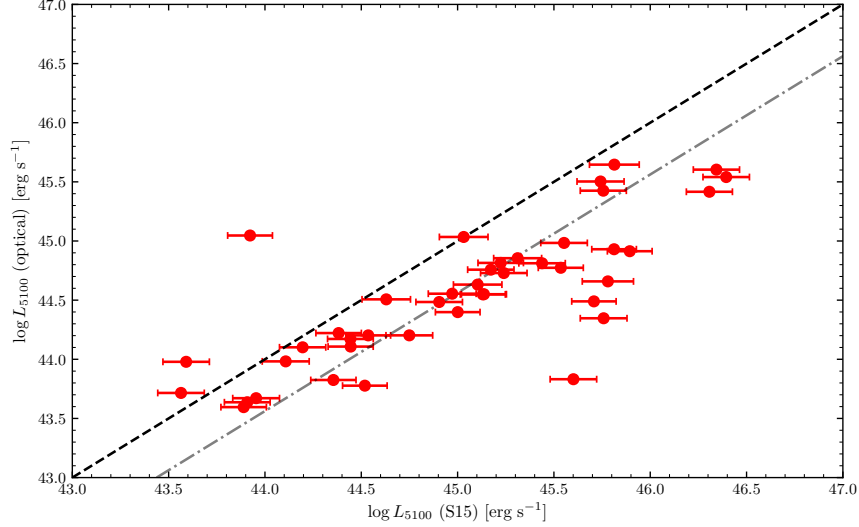


Figure 13. Comparison between the optical-derived 5100 Å luminosity and the IR-derived one. The dashed line represents the one-to-one relation. Overall, the former is smaller than the latter by a factor of 2.74 (indicated by the dash-dotted line), which might indicate the disk emission is anisotropic.

APPENDIX

A. ENERGY BUDGET

In Section 2, we interpolate between the SDSS *ugriz* bands or between the Palomar B-band and 2MASS J-band (in the cases of no SDSS counterparts) to derive the rest-frame 5100 Å luminosity (hereafter $L_{5100}(\text{optical})$). The same quantity can also be inferred from our IR decomposition results. First, we use the methodology in Section 3.2 of Siebenmorgen et al. (2015) and our best-fitting AGN templates to drive the bolometric luminosities for our AGNs (hereafter $L_{\text{bol}}(\text{S15})$). Second, we use the spectral shape of the primary AGN emission adopted by Siebenmorgen et al. (2015, see their Eq. 2) to calculate the rest-frame 5100 Å luminosity (hereafter $L_{5100}(\text{S15})$). A comparison between the two 5100 Å luminosities is presented in Figure 13.

There is an evident correlation between $L_{5100}(\text{optical})$ and $L_{5100}(\text{S15})$. However, $L_{5100}(\text{optical})$ is systematically smaller (by a median factor of ~ 2.74) than $L_{5100}(\text{S15})$. This discrepancy might be understood as follows. The optical emission is widely believed to be produced by the optically thick but geometrically thin accretion disk (Shakura & Sunyaev 1973). That is, the optical emission is expected to be highly anisotropic and anti-correlate with the viewing angle (θ). The line-of-sight effect has been considered in $L_{5100}(\text{S15})$. Therefore, the ratio of $L_{5100}(\text{optical})$ to $L_{5100}(\text{S15})$ actually measures our viewing angle, i.e., $\theta \sim 68$ degrees. This estimation of the viewing angle is roughly consistent with our SED decomposition results (see panel (e) of Figure 8). In addition, optical extinction (which effectively reduces our estimations of $L_{5100}(\text{optical})$) due to line-of-sight dust might also be partially responsible for the discrepancy.

B. FITTING THE SEDS WITH AGN TEMPLATES ALONE

For each of the 42 sources, we also try to fit the observed SED with the AGN templates alone (i.e., fixing $c_2 \equiv 0$), with one example shown in Figure 14. **Fig. Set 2. displays the best-fitting results with the AGN templates alone for all our 42 sources.** It is clear that, without a galaxy component, the best-fitting result is poor and unacceptable ($\chi^2_{\nu} = 2273.214$). This is because the best-fitting AGN template cannot account for the FIR data. In fact, for each of the 42 sources, the best-fitting result can be significantly improved if we add a galaxy component (see the second and third columns of Table 2).

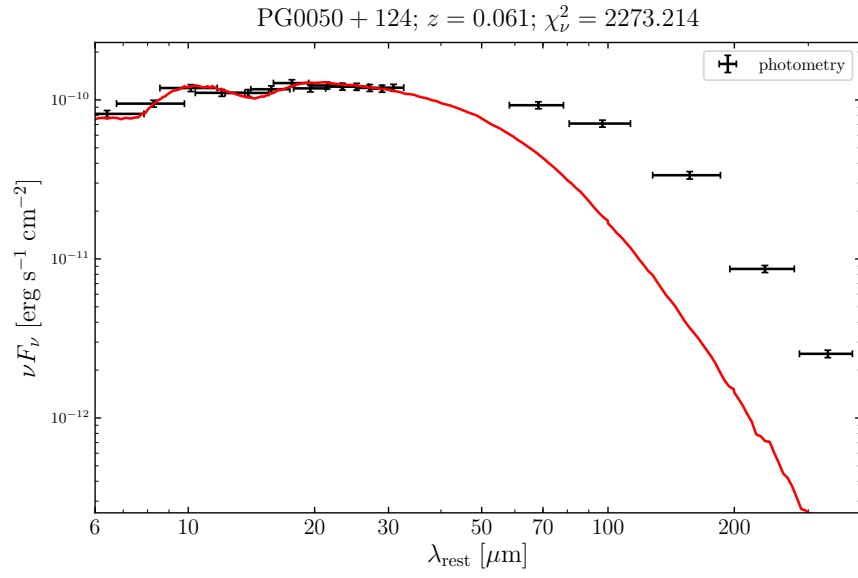


Figure 14. An illustration of our SED-fitting results with AGN templates alone. Without a galaxy component, the best-fitting AGN template significantly underestimates the observed FIR emission; that is, this fit is unacceptable ($\chi^2_\nu = 2273.214$). The complete figure set that contains the best-fitting results of all 42 sources is available in the online journal.